Nanoscale

PAPER

View Article Online
View Journal | View Issue

Cite this: *Nanoscale*, 2018, **10**, 18734

Three-dimensionally ordered mesoporous multicomponent (Ni, Mo) metal oxide/N-doped carbon composite with superior Li-ion storage performance†

Se Hwan Oh,‡[a] Jin Koo Kim,‡[b] Yun Chan Kang *[b] and Jung Sang Cho*[a]

Received 20th August 2018,
Accepted 21st September 2018

DOI: 10.1039/c8nr06727a

rsc.li/nanoscale

Among the various nanostructures, porous materials with controlled pore structures have been widely used for designing transition metal-based anode materials for lithium-ion batteries, because they provide good access to electrolyte and can effectively accommodate stress arising from volume changes. In particular, ternary transition metal oxide materials containing nanovoids, arranged with high degree of periodicity, are ideal for enhancing lithium-ion storage capability. In this study, we provide a method using spray pyrolysis for the synthesis of mesoporous multicomponent metal oxide microspheres containing Ni and Mo components and N-doped carbon, in which three-dimensionally ordered 40 nm-sized mesopores are interconnected. During the synthesis, polystyrene nanobeads are used as a sacrificial template and are readily eliminated *via* thermal decomposition. Increased concentrations of polystyrene nanobeads enables the formation of open channels throughout the microspheres. When employed as a lithium-ion battery anode, the mesoporous multicomponent metal oxide microspheres containing Ni and Mo components and N-doped carbon exhibit high reversible capacity, good cycling stability, and excellent rate performance. After 1000 cycles, the microspheres deliver a discharge capacity of 693 mA h g^{-1} at a current density of 1.0 A g^{-1}.

Introduction

The use of transition metal oxides and their derivatives as anode materials for advanced lithium-ion batteries (LIBs) has been widely studied because of their high electrochemical activities owing to complex chemical compositions and valence states.[1–10] Although transition metal oxide-based electrodes typically have 2–3-times higher specific capacity than carbon-based electrodes, their widespread use has been hindered by the large volume change during lithiation and delithiation, which eventually destroys the electrode after a few cycles.[11–15] To overcome this issue, various nanostructures with well-defined internal voids have been proposed to accommodate the stress from volume changes and maximize surface area.[16–28] These rationally designed nanostructures, including hollow,[16] yolk–shell,[17] multi-shell,[18] multi-room,[19] and porous structures,[20] have been synthesized by eliminating templates such as silica, carbon, and organic ligands. In particular, 3-dimensionally ordered mesoporous (3-DOM) structures with open channels for energy storage have received significant interest because they provide good access to electrolytes with much shorter diffusion lengths.[29–33] For example, Liu *et al.* prepared ordered mesoporous NiO by a nanocasting method using mesoporous silica as a hard template.[29] Hu *et al.* synthesized 3D MoS_2-reduced graphene oxide/hollow carbon sphere composites, in which a hollow void was obtained by etching silicate.[30] Choi *et al.* synthesized 3D MoS_2-graphene and $MoSe_2$-CNT microspheres by spray pyrolysis *via* thermal decomposition of polystyrene (PS) nanobeads, both of which exhibited excellent sodium ion storage.[31,32] McNulty *et al.* prepared crystalline macroporous GeO_2 inverse opal *via* the infilling of a sacrificial PS template with Ge precursor.[33] However, most studies have focused on nanostructuring binary metal oxides and chalcogenides. When applied as the anode materials of LIBs, ternary metal oxides with two different metal cations can outperform binary metal oxides due to the synergistic effects of the multiple metal species.[34,35] For example, hybridizing Co_3O_4 and SnO_2 can enhance the reversible capacity and cyclability, because the presence of Co nano-

[a]*Department of Engineering Chemistry, Chungbuk National University, Chungbuk 361-763, Republic of Korea. E-mail: jscho@cbnu.ac.kr; Fax: (+82) 43-262-2380*
[b]*Department of Materials Science and Engineering, Korea University, Anam-Dong, Seongbuk-Gu, Seoul 136-713, Republic of Korea. E-mail: yckang@korea.ac.kr; Fax: (+82) 2-928-3584*

†Electronic supplementary information (ESI) available. See DOI: 10.1039/c8nr06727a

‡These authors contributed equally to the work.

particle improves the reversibility of the reduction reaction of Li_2O and inhibits coarsening of Sn nanoparticles during lithiation and delithiation.[34] To the best of our knowledge, multicomponent oxide-based LIB anode materials with three-dimensionally ordered mesopores, especially those hybridized with carbon, are rarely reported. Among various ternary transition metal oxides, $NiMoO_4$ has been highlighted as a promising anode material candidate for LIBs because it provides multiple oxidation states, large cell parameters, and relatively high electrical conductivity due to the presence of Mo.[36,37] However, without proper architecture, $NiMoO_4$ still suffers from poor kinetics and structural instability which significantly limits its practical use.

In this study, we report the preparation of mesoporous multicomponent metal oxides containing Ni and Mo components with N-doped carbon (denoted as NiMo/C-300 composite) by a spray pyrolysis process. Using thermal decomposition of PS nanobeads during synthesis, 40 nm-sized mesopores with open channels were successfully formed. Furthermore, N-doped carbon was successfully incorporated into the composite to enhance the electrical conductivity. Combined with a rational architecture, synthesized mesoporous composite microspheres exhibited superior electrochemical properties as an anode material for LIBs.

Experimental

Sample preparation

Mesoporous Ni–Mo–C composite microspheres were prepared by spray pyrolysis and subsequent heat treatment. The spray solution was prepared by dissolving 10.0 g of $Ni(NO_3)_2{\cdot}6H_2O$ (97%, Junsei), 6.88 g of $(NH_4)_6Mo_7O_{24}{\cdot}4H_2O$ (98%, Daejung), and 4.0 g of poly(vinylpyrrolidone) (PVP; M_w = 40 000, Junsei) in 200 mL of distilled water. Then, 200 mL of 100 nm-sized polystyrene (PS) nanobead colloidal solution (100 mg mL^{-1}) was added and sonicated for 1 h to obtain a yellow-green colloidal solution. The molar ratio of Ni ions to Mo ions in the spray solution was 1 : 1. A quartz reactor was used to carry the droplets generated by the ultrasonic nebulizer with N_2 gas (carrier gas) supplied at a flow rate of 10 L min^{-1}. The temperature of the furnace was 700 °C. The product was collected in the fume hood and post-treated in a box-furnace at 300, 400, and 500 °C for 1 h under ambient air with a ramping rate of 5 °C min^{-1}. The obtained samples were denoted NiMo/C-300, NiMo-400, and NiMo-500, respectively.

Characterization techniques

The morphologies of the samples were analyzed by field emission scanning electron microscopy (FE-SEM; Zeiss, Ultra Plus) and field emission transmission electron microscopy (FE-TEM; JEOL, JEM-2100F). Crystal structure analysis was conducted by X-ray diffraction (XRD; X'Pert PRO MPD) using Cu-K_α radiation (λ = 1.5418 Å). The composition and chemical environment of the samples were investigated by X-ray photoelectron spectroscopy (XPS; Thermo Scientific K-Alpha) with focused monochromatic Al-K_α radiation at 12 kV and 20 mA. The specific surface area and pore size of the samples were measured by Brunauer–Emmett–Teller (BET) analysis (TriStar 3000). Carbon content of the samples was determined by thermogravimetric analysis (TGA; SDT Q600), which was conducted in air with a ramping rate of 10 °C min^{-1}. Nitrogen and carbon contents of the sample were analyzed elemental analyzer (EA; vario MICRO cube).

Electrochemical measurements

The capacities and cycle properties of the samples were measured using 2032-type coin cells. The cell electrodes were prepared using slurry consisting of 70 wt% active anode material, 20 wt% carbon black (Super-P) as a conductive material, and 10 wt% binder composed of sodium carboxymethyl cellulose (CMC) on a copper foil. Lithium metal and microporous poly(propylene) film were used as the counter electrode and separator, respectively. The electrolyte was created by dissolving 1 M $LiPF_6$ in a mixture of fluoroethylene carbonate and dimethyl carbonate (FEC/DMC, 1 : 1 v/v). The entire cell was assembled in an argon atmosphere in a glove box. The charge/discharge characteristics of the samples were measured at various current densities in the voltage range of 0.001–3.0 V. The size of the negative electrode containing the mesoporous $NiMoO_4$-MoO_2-Ni/N-doped C microspheres were 1.4 cm × 1.4 cm, and the mass loading was approximately 0.98 mg cm^{-2}. Cyclic voltammetry measurements were performed at a scan rate of 0.1 mV s^{-1} between 0.001 and 3.0 V. Electrochemical impedance spectra were analyzed in the frequency range between 100 kHz and 10 MHz at room temperature with a signal amplitude of 5.0 mV.

Results and discussion

The formation mechanism of mesoporous multicomponent metal oxides containing Ni and Mo components with and without carbon prepared by a spray pyrolysis and subsequent oxidation process is described in Scheme 1. The ultrasonic nebulizer generates a mist of droplets containing metal (Ni and Mo) salts, PVP, and PS nanobeads. The composition of the droplets is virtually uniform since the spray solution is a

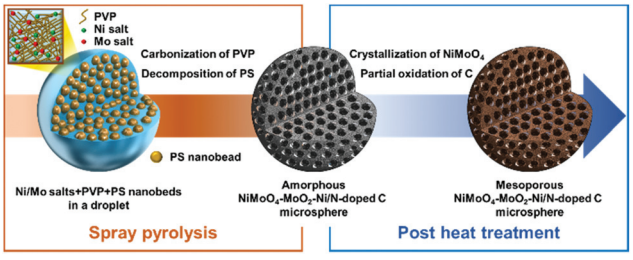

Scheme 1 Formation mechanism of mesoporous $NiMoO_4$-MoO_2-Ni/N-doped C microsphere.

homogeneous colloid. The water vaporizes as soon as the droplets reach the quartz reactor, and subsequent melting of the metal salts and PVP forms balls of molten metal salt-PVP composite in which thousands of PS nanobeads are evenly embedded. Further exposure to a temperature of 700 °C results decomposition of the metal salts and PS nanobeads as well as the carbonization of PVP. Thermal decomposition of the PS nanobeads creates mesopores with open channels throughout the microspheres, resulting in mesoporous Ni–Mo–C composite microspheres with mixed crystal structures of Ni, MoO_2, and $NiMoO_4$ phases. The residence time of the microspheres in the quartz reactor during the entire process is about 14 s. Mesoporous NiMo/C-300 composites with carbon material and carbon-free $NiMoO_4$ microspheres were synthesized by a one-step post-treatment under an air atmosphere at 300 and 400 °C, respectively.

The SEM image and XRD pattern of the mesoporous precursor microspheres synthesized by the one-step spray pyrolysis process are shown in Fig. S1.† The SEM image in Fig. S1a† clearly shows a uniform distribution of mesopores over the microspheres. Average pore diameter was around 40 nm, which was much smaller than that of the PS nanobeads (100 nm). Contraction of the microspheres during the decomposition process caused shrinkage of the pore diameter. The XRD pattern in Fig. S1b† shows broad diffraction peaks, indicating the presence of a mixed phase consisting of $NiMoO_4$, MoO_2, and Ni. Carbothermal reduction induced by the high temperature of 700 °C caused the formation of Ni and MoO_2 phases. The as-prepared precursor microspheres were post-treated at various temperatures under ambient air to oxidize Ni and MoO_2 and optimize the carbon content for use as the anode material for LIBs.

The SEM and low-resolution TEM images of the mesoporous composite microspheres (denoted as NiMo/C-300) obtained by oxidation of the precursor microspheres at 300 °C are shown in Fig. 1a–c. The internal and external mesoporous structures were maintained and severe crystal growth was not observed. A uniform distribution of mesopores with open channels throughout the microsphere is indicated by the very fine mosaic pattern with vivid contrast. The high-resolution TEM image in Fig. 1d reveals that the composite is mostly nanocrystalline, which was already inferred from the broad diffraction peaks shown in Fig. S2.† The inset image in Fig. 1d indicates the formation of $NiMoO_4$ nanocrystals, though the lattice fringe is not very distinctive. The selected-area electron diffraction (SAED) pattern in the inset of Fig. 1d exhibits several rings that are indicative of the presence of Ni, MoO_2, and $NiMoO_4$ phases. Formation of a multi-phase was also supported by the XRD pattern of NiMo/C-300 in Fig. S2.† The weakly developed peaks indicate low crystallinity of the chemical species in the composite, as already seen in the blurry lattice image in Fig. 1d. The elemental mapping images in Fig. 1e confirmed the homogeneous distribution of Ni, Mo, O, C, and N, where N was doped into carbon during the carbonization of PVP. This implies that ultrafine nanocrystals having different phases are homogeneously mixed over the microsphere, so any degradation of electrochemical performance by phase segregation is not likely to be of concern. Incorporation with N-doped carbon is effective for enhancing both the electrical conductivity and the structural stability of the composite. Elemental analysis of NiMo/C-300 was carried out to confirm the accurate amount of C and N in NiMo/C-300 (Table S1†). According to the result, the total amount of C and N in NiMo/C-300 were about 15.3 and 2.4 wt%, respectively. Since the formation of metal nitrides was not observed, it can be inferred that N atoms were doped in the carbon matrix. Therefore, the N content in N-doped carbon was calculated to be 13.6 wt%. Previous reports demonstrated that N-doped carbon generally contains 2–16 wt% of nitrogen, which is consistent with our result.[37–40]

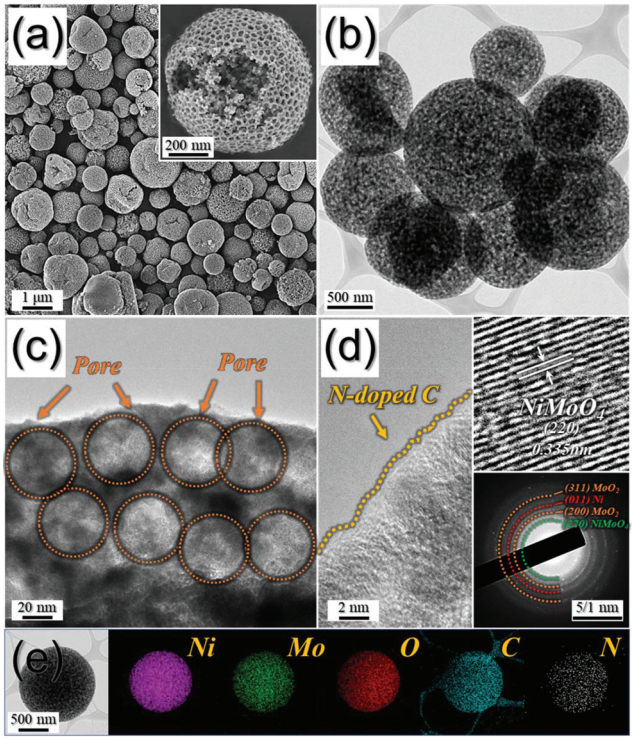

Fig. 1 Morphologies, SAED pattern, and elemental mapping images of NiMo/C-300 microspheres prepared by spray pyrolysis and oxidation at 300 °C: (a) SEM image, (b,c) TEM images, (d) HR-TEM images and SAED pattern, and (e) elemental mapping images.

The chemical state of NiMo/C-300 was characterized by XPS. The survey spectrum in Fig. 2a had obvious peaks of Ni 2p, Mo 3d, O 1s, N 1s, and C 1s. The Mo 3d spectrum in Fig. 2b shows intense peaks centered at 232.8 and 235.9 eV, which correspond to Mo $3d_{5/2}$ and Mo $3d_{3/2}$, respectively.[41,42] Deconvolution of the peaks revealed the presence of Mo^{6+} (centered at 232.8 and 235.9 eV) and Mo^{4+} (centered at 232.08 and 234.86 eV) states, indicating the co-existence of MoO_2 and $NiMoO_4$ phases.[43] The Ni 2p spectrum in Fig. 2c contains two pronounced peaks corresponding to Ni $2p_{3/2}$ and Ni $2p_{1/2}$ doublets and their satellite peaks. Deconvolution of the peaks confirmed the presence of Ni^{2+} (centered at 856.4 and 873.9

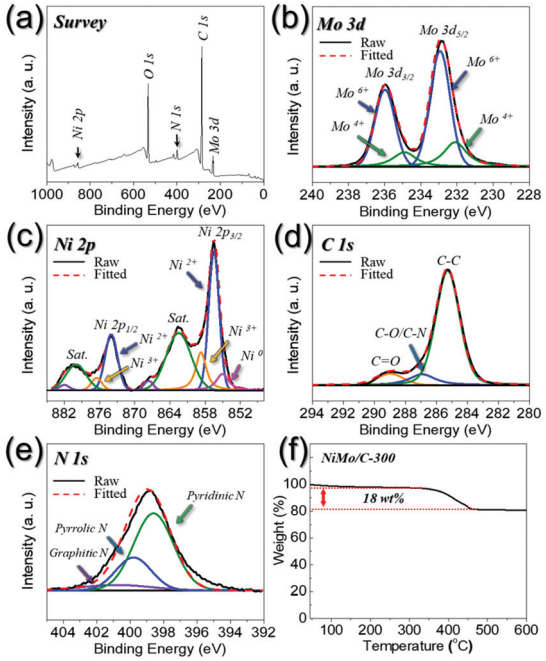

Fig. 2 (a) XPS survey spectrum and core-level XPS spectra of (b) Mo 3d, (c) Ni 2p, (d) C 1s, (e) N 1s, and (f) TG curve of NiMo/C-300.

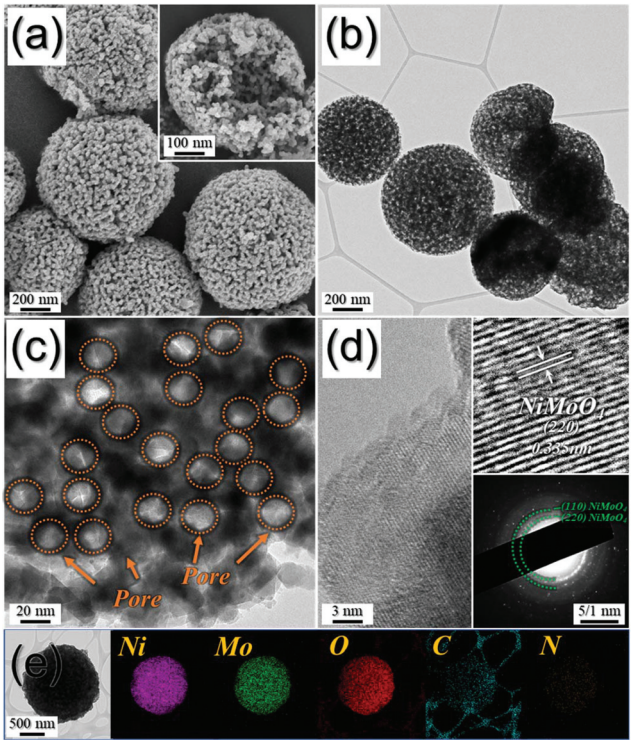

Fig. 3 Morphologies, SAED pattern, and elemental mapping images of NiMo-400 prepared by spray pyrolysis and oxidation at 400 °C: (a) SEM image, (b,c) TEM images, (d) HR-TEM images and SAED pattern, and (e) elemental mapping images. Composite nanobelts prepared by electrospinning process.

eV), Ni^{3+} (centered at 858.7 and 876.5 eV), and Ni^{0} (centered at 855.1 eV).[44–46] The C 1s spectrum in Fig. 2d contains three peaks, corresponding to C–C (sp^3), C–O/C–N, and C=O functionalities at 285.2, 286.9, and 288.9 eV, respectively.[43,44] In the N 1s spectrum (Fig. 2e), three types of N species were present. Pyridinic N (398.5 eV) was the most dominant compared with pyrrolic N (399.8 eV) and graphitic N (400.5 eV), and these accounted for 73, 23, and 4% of the N configuration, respectively.[47] The carbon content of NiMo/C-300 estimated by TG analysis is shown in Fig. 2f. Excluding a small weight decrease at 150 °C, which was attributed to the evaporation of adsorbed water, the weight of the composite decreased by 18 wt%. Although the presence of Ni, MoO_2, and $NiMoO_4$ in NiMo/C-300 was confirmed by XRD, exact proportions of the species was unknown. The weight gain associated with the stoichiometric reaction of Ni and MoO_2 with two oxygen atoms to form $NiMoO_4$ is around 17 wt%. Since the composite already contained a substantial amount of $NiMoO_4$, weight gain by the oxidation of the metal species is not significant enough to account for the weight loss by the combustion of carbon. Therefore, the carbon content of NiMo/C-300 can be regarded as slightly more than 18 wt%.

To prepare carbon-free samples with higher crystallinity, oxidation of mesoporous precursor microspheres was conducted at higher temperatures. The SEM and low-resolution TEM images of mesoporous $NiMoO_4$ microspheres oxidized at 400 °C (denoted as NiMo-400) are shown in Fig. 3a–c. Compared with NiMo/C-300, NiMo-400 had larger grains and smaller pore sizes. In addition, several mesopores were blocked. This indicated that oxidation at 400 °C resulted in crystal growth driven by elimination of carbon, which consequentially collapsed and blocked the PS-derived pores. The clear lattice fringe in Fig. 3d corresponded to (220) plane of $NiMoO_4$ with high crystallinity, whose presence was further verified by SAED and XRD patterns in Fig. 3d and S2.†[48] The elemental mapping images in Fig. 3e confirmed the presence of Ni, Mo, and O. Signals from C and N were barely detected, indicating that the N-doped carbon was virtually completely decomposed by combustion during the oxidation. This was also validated by the TG curve in Fig. S3a,† where weight loss by the combustion of carbon with respect to elevating temperature was not detected. The chemical state of NiMo-400 was characterized by XPS, and the results are shown in Fig. S4.† The survey spectrum in Fig. S4a† showed the presence of Ni 2p, Mo 3d, and O 1s. The C 1s peak was not found, indicating the complete combustion of carbon species. The Mo 3d spectrum in Fig. S4b† revealed intense peaks centered at 232.0 and 235.2 eV, which corresponded to Mo $3d_{5/2}$ and Mo $3d_{3/2}$ of the Mo^{6+} oxidation state, respectively.[40,41] The Ni 2p spectrum in Fig. S4c† was similar to that of NiMo/C-300 in Fig. 2c. The Ni $2p_{3/2}$ peak could be deconvoluted into two peaks centered at 856.4 and 857.6 eV, which were attributed to the Ni^{2+} and Ni^{3+} oxidation states, respectively. In the same way, deconvolution of Ni $2p_{1/2}$ confirmed the Ni^{2+} and Ni^{3+} oxidation states centered at 873.9 and 875.9 eV, respectively.[44,45]

The morphological analysis of mesoporous $NiMoO_4$ microspheres oxidized at 500 °C (denoted as NiMo-500) is shown in Fig. 4. Markedly, considerable crystal growth and sintering between the grains occurred, as seen in the SEM and TEM images in Fig. 4a–c. Although the overall mesoporous structure was still preserved to some extent, a large amount of pores was blocked by sintering. The clear lattice fringe, SAED pattern, and sharply defined XRD pattern in Fig. 4d and S2† confirmed the formation of a $NiMoO_4$ single phase with a crystal size of 31 nm, which is higher than those of NiMo/C-300 (21 nm) and NiMo-400 (22 nm). Elemental mapping images in Fig. 4e indicated the presence of Ni, Mo, and O, where N-doped carbon was hardly remaining, similar to NiMo-400. The flat TG curve in Fig. S3b† also demonstrated the absence of carbon species.

The N_2-adsorption/desorption isotherms of the samples were compared to investigate the effect of oxidation temperature on the amount of surface area, and the results are shown in Fig. S5a.† The BET surface areas of NiMo/C-300, NiMo-400, and NiMo-500 were measured to be 84, 43, and 27 $m^2\ g^{-1}$, respectively. The high surface area of NiMo/C-300 was ascribed to the presence of N-doped carbon and ultrafine nanocrystals. Predictably, NiMo-500 had the lowest surface area because severe crystal growth and sintering at a high oxidation temperature inevitably reduced the surface area. The Barrett–Joyner–Halenda (BJH) pore size distribution of NiMo/C-300 shown in Fig. S5b† suggests that the majority of the pores have sizes between 10 to 40 nm. This result agrees with the average pore size measured from the SEM and TEM images in Fig. 1a–c.

The electrochemical properties of the mesoporous multicomponent metal oxides containing Ni and Mo components with and without carbon as anode materials for LIBs are compared and analyzed in Fig. 5. The first five CV curves of NiMo/C-300 obtained at a scan rate of 0.1 mV s^{-1} over a potential range of 0.001–3.0 V are depicted in Fig. 5a. In the first cathodic scan, broad peaks at around 1.6 and 0.5 V were observed, which could be attributed to the formation of a solid-electrolyte interphase (SEI) layer and the reduction of oxide species ($NiMoO_4$ and MoO_2) into Ni and Mo nanocrystals, respectively.[41,49,50] The peak at 0.05 V is due to the reaction of Li^+ ions with carbon in the composite.[51–53] Meanwhile, in the anodic scans, a reversible peak located at 1.4 V indicates the oxidation of Ni and Mo to NiO and MoO_2, respectively. Another peak at 1.7 V indicates the partial oxidation of MoO_2 to MoO_3, since the composite had both MoO_2 and $NiMoO_4$.[41,49,50] In the subsequent cycles, two redox peak pairs appeared at 0.7/1.4 and 1.3/1.7 V, which corresponded to the redox reaction of NiO/MoO_2 and MoO_3, respectively.[41,49,50] The curves overlapped substantially, indicating the high reversibility of the redox reactions and chemical stability of the composite. The CV curves of NiMo-400 and NiMo-500 are shown in Fig. S6.† The shapes of the curves were similar to those of NiMo/C-300, with more distinctive peak intensities due to the higher crystallinity and absence of carbon. The initial discharge/charge profiles of NiMo/C-300, NiMo-400, and NiMo-500 obtained at a current density of 1.0 A g^{-1} are shown in Fig. 5b. The discharge pro-

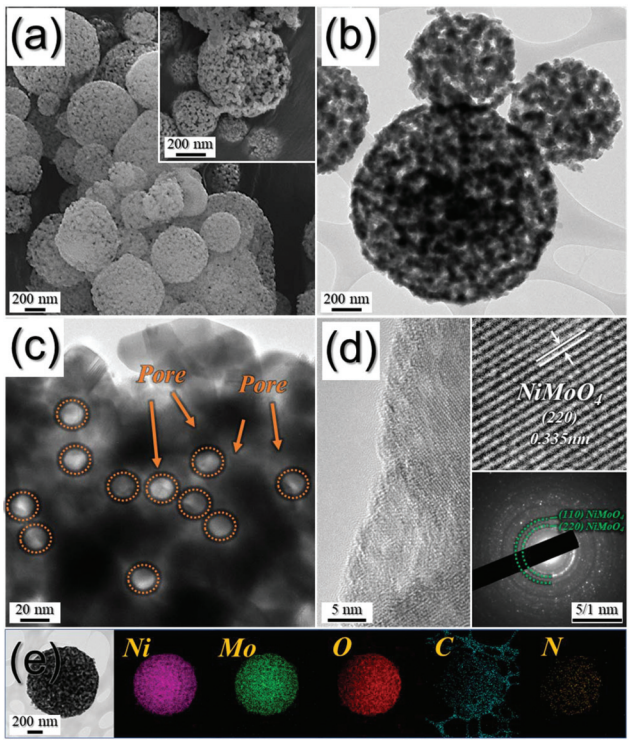

Fig. 4 Morphologies, SAED pattern, and elemental mapping images of NiMo-500 prepared by spray pyrolysis and oxidation at 500 °C (a) SEM image, (b,c) TEM images, (d) HR-TEM images and SAED pattern, and (e) elemental mapping images.

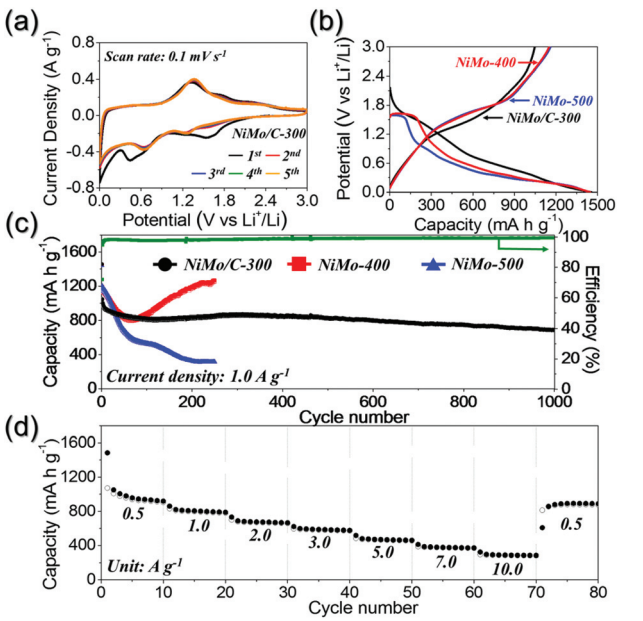

Fig. 5 Electrochemical properties of mesoporous Ni–Mo–C composite microspheres oxidized at various temperatures: (a) CV curves of NiMo/C-300, (b) initial charge and discharge profiles, (c) cycling performances, and (d) rate performance of NiMo/C-300.

files show plateaus located at around 1.6 and 0.6 V, which corresponded to the reduction peaks of the CV curves. The charge profiles show plateaus from 1.4 to 1.8 V that corresponded to the oxidation of Ni and Mo nanocrystals. It is noteworthy that NiMo/C-300 showed the least polarization between the discharge and charge plateau, indicating that the kinetics of NiMo/C-300 are better than NiMo-400 and NiMo-500. The kinetics of the electrodes are known to be related to the internal resistances, Li^+ ion diffusivity, electrical conductivity, and interfacial charge transfer.[54] The improved kinetics of NiMo/C-300 can be attributed to the mesoporous structure with an optimum pore size and channel and higher electrical conductivity of the N-doped carbon derived from PVP.[55] The cycling performances of NiMo/C-300, NiMo-400, and NiMo-500 at a current density of 1.0 A g^{-1} are shown in Fig. 5c. The initial discharge capacities of NiMo/C-300, NiMo-400, and NiMo-500 were 1458, 1447 and 1442 mA h g^{-1}, respectively, and their corresponding charge capacities were 1050, 1151, and 1163 mA h g^{-1}. Also, the initial coulombic efficiencies of the samples were 72, 80, and 80%, respectively. Note that the irreversible capacity loss of NiMo/C-300 was similar to that of NiMo-400. This phenomenon was attributed to the greater structural stability of NiMo/C-300 over NiMo-400 due to restricted crystal growth, although carbonaceous materials usually exhibit large irreversible capacity loss. Accordingly, NiMo-500, whose structural stability was heavily deteriorated by severe crystal growth, exhibited the poorest coulombic efficiency. The reversible capacity of NiMo/C-300 was stable over 1000 cycles, exhibiting a high discharge capacity of 693 mA h g^{-1} at the 1000th cycle.

This exceptional stability was attributed to the existence of interconnected pores with optimum size and N-doped carbon that effectively accommodated the volume changes during lithiation/delithiation and restricted the overgrowth of metal oxide nanocrystals. On the other hand, NiMo-400 and NiMo-500 suffered severe capacity loss over the first 70 cycles. This was caused by the pulverization of the composite, which was attributed to the overgrowth of grains that frustrated effective stress alleviation. The capacity increase of NiMo-400 after the 70th cycle was related to the deposition of an additional SEI layer on the newly exposed cracked surface formed by pulverization. The rate performance of NiMo/C-300 is shown in Fig. 5d. The discharge capacities of NiMo/C-300 at the current densities of 0.5, 1.0, 2.0, 3.0, 5.0, 7.0, and 10.0 A g^{-1} were 918, 788, 665, 577, 460, 371, and 284 mA h g^{-1}, respectively. The composite recovered a stable discharge capacity of 866 mA h g^{-1} when the current density returned to 0.5 A g^{-1}, which corresponded to a capacity recovery of 95%. The morphologies of NiMo/C-300, NiMo-400, and NiMo-500, after the 100th cycle, are shown in Fig. 6. NiMo/C-300 maintained its spherical shape and pore structure at a high current density of 1.0 A g^{-1}, as shown in Fig. 6a and b. On the other hand, NiMo-400 (Fig. 6c and d) and NiMo-500 (Fig. 6e and f) were completely pulverized. It can be inferred that N-doped carbon in NiMo/C-300 effectively relieved the mechanical stress from volume expansion during cycling.

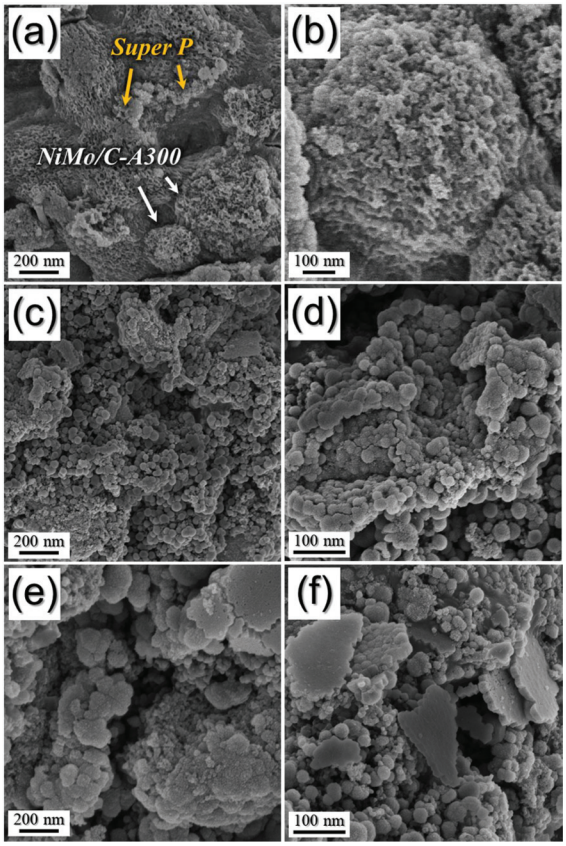

Fig. 6 Morphologies of (a,b) NiMo/C-300, (c,d) NiMo-400, and (e,f) NiMo-500 after 100th cycle.

The electrochemical properties of our sample were also compared with other previously reported $NiMoO_4$-based materials with various morphologies, as summarized in Table S2.† Compared with the previously reported materials, our sample exhibited the enhanced cycling stability at high current density. The outstanding rate performance and long cycling stability were stemmed from the interconnected mesoporous structure along with the N-doped carbon matrix, which facilitated electrolyte penetration for Li^+ ion diffusivity and accommodated the volume changes during cycling.

The superior Li^+ ion storage of NiMo/C-300 was further investigated by EIS measurements.[56–59] The Nyquist impedance plots of NiMo/C-300, NiMo-400, and NiMo-500, obtained right after the cell assembly, are shown in Fig. 7a. NiMo-400 and NiMo-500 with high crystallinity exhibited lower R_{ct} value than NiMo/C-300, because pure $NiMoO_4$ has higher conductivity than non-stoichiometric multicomponent (Ni,Mo) phases.[60] On the other hand, the Nyquist plots of the samples obtained after the 1st and 100th cycles at a fully charged state exhibited a sharp contrast, as shown in Fig. 7b–d. The R_{ct} value of NiMo/C-300 barely changed (from 29.9 to 36.9 Ω), whereas those of NiMo-400 and NiMo-500 increased from 28.6 to 46.4 Ω and from 43.6 to 63.0 Ω, respectively. This proves the high structural stability of NiMo/C-300 conferred by its interconnected mesopores with optimum size and N-doped carbon

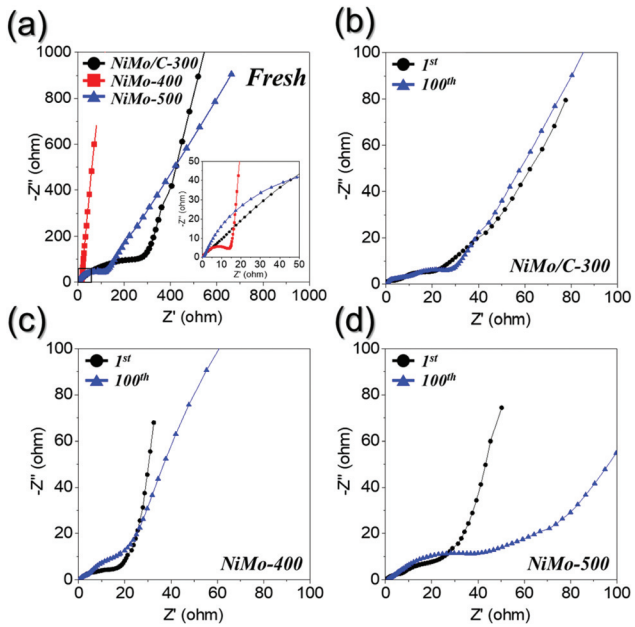

Fig. 7 Nyquist impedance plots of NiMo/C-300, NiMo-400, and NiMo-500: (a) before cycling and after 1st and 100th cycle of (b) NiMo/C-300, (c) NiMo-400, and (d) NiMo-500.

that alleviated the stress from the volume change and agglomeration during the repeated lithiation/delithiation processes.

Conclusions

In this work, the superior electrochemical properties of mesoporous multicomponent metal oxides of Ni and Mo components with N-doped carbon as an anode material for LIBs were investigated. Such rationally designed microspheres were synthesized by scalable spray pyrolysis and calcination in air by employing PS nanobeads as porogen. Due to the structural stability conferred by the unique architecture and excellent electrochemical properties of ternary transition metal oxides ascribed to the multiple valence states, mesoporous multicomponent metal oxides containing Ni and Mo components with N-doped carbon exhibited outstanding cycling and rate performances. The synthetic method introduced in this work could be tailored for other applications.

Conflicts of interest

There are no conflicts to declare.

Acknowledgements

This work was supported by the National Research Foundation of Korea (NRF) grant funded by the Korea government (MSIP) (NRF-2018R1A4A1024691, NRF-2017M1A2A2087577, and NRF-2017R1A4A1014806).

References

1 Y. Shi, B. Guo, S. A. Corr, Q. Shi, Y.-S. Hu, K. R. Heier, L. Chen, R. Seshadri and G. D. Stucky, *Nano Lett.*, 2009, **9**, 4215–4220.
2 J. S. Cho, Y. J. Hong and Y. C. Kang, *ACS Nano*, 2015, **9**, 4026–4035.
3 H. J. Fan, U. Cosele and M. Zacharias, *Small*, 2007, **3**, 1660–1671.
4 M. F. Hassan, Z. P. Guo, Z. Chen and H.-K. Liu, *J. Power Sources*, 2010, **195**, 2372–2376.
5 K. Cao, P. Li, Y. Zhang, T. Chen, X. Wang, S. Zhang and J. Liu, *Nano Energy*, 2017, **40**, 187–194.
6 C. Guan, Y. Wang, M. Zacharias, J. Wang and H. J. Fan, *Nanotechnology*, 2014, **26**, 014001.
7 S.-H. Ng, J. Wang, D. Wexler, K. Konstantinov, Z.-P. Guo and H. K. Liu, *Angew. Chem., Int. Ed.*, 2006, **45**, 6896–6899.
8 J.-S. Park, J. S. Cho, J. H. Kim, Y. J. Choi and Y. C. Kang, *J. Alloys Compd.*, 2016, **689**, 554–563.
9 B. Wang, J. L. Cheng, Y. P. Wu, D. Wang and D. N. He, *Electrochem. Commun.*, 2012, **23**, 5–8.
10 Q. Li, P. Wang, Q. Feng, M. Mao, J. Liu, S. X. Mao and H. Wang, *Chem. Mater.*, 2014, **26**, 4102–4108.
11 J. S. Cho, S. Y. Lee, H. S. Ju and Y. C. Kang, *ACS Appl. Mater. Interfaces*, 2015, **7**, 25641–25647.
12 Y. Dong, S. Liu, Z. Wang, Y. Liu, Z. Zhao and J. Qiu, *RSC Adv.*, 2015, **5**, 8929–8932.
13 L. A. Riley, A. S. Cavanagh, S. M. George, Y. S. Jung, Y. Yan, S. H. Lee and A. C. Dillon, *ChemPhysChem*, 2010, **11**, 2124–2130.
14 J. M. Won, J. H. Kim, Y. J. Choi, J. S. Cho and Y. C. Kang, *Ceram. Int.*, 2016, **42**, 5461–5471.
15 Y. Liu, P. Li, Y. Wang, J. Liu, Y. Wang, J. Zhang, M. Wu and J. Qiu, *J. Alloys Compd.*, 2017, **695**, 2612–2618.
16 J. S. Cho, J. M. Won, J.-H. Lee and Y. C. Kang, *Nanoscale*, 2015, **7**, 19620–19626.
17 Y. J. Hong and Y. C. Kang, *Small*, 2015, **11**, 2157–2163.
18 G. D. Park, J.-H. Lee, J.-K. Lee and Y. C. Kang, *Nano Res.*, 2014, **7**, 1738–1748.
19 J. S. Cho, J. M. Won, J.-K. Lee and Y. C. Kang, *Nano Energy*, 2016, **26**, 466–478.
20 J. Jiang, Y. Li, J. Liu, X. Huang, C. Yuan and X. W. D. Lou, *Adv. Mater.*, 2012, **24**, 5166–5180.
21 L. Li, X. Yin, S. Liu, Y. Wang, L. Chen and T. Wang, *Electrochem. Commun.*, 2010, **12**, 1383–1386.
22 P. Liu, W. Lei, X. Xia and Q. Hao, *ChemElectroChem*, 2017, **4**, 2068–2074.
23 S. H. Oh, J.-S. Park, M. S. Jo, Y. C. Kang and J. S. Cho, *Chem. Eng. J.*, 2018, **347**, 889–899.
24 J. Wang, N. Yang, H. Tang, Z. Dong, Q. Jin, M. Yang, D. Kisailus, H. Zhao, Z. Tang and D. Wand, *Angew. Chem., Int. Ed.*, 2013, **125**, 6545–6548.
25 Z. Wang, L. Zhou and X. W. D. Lou, *Adv. Mater.*, 2012, **24**, 1903–1911.
26 S. A. Corr, *Nanoscience*, 2016, **3**, 31–56.

27 X. M. Yin, C. C. Li, M. Zhang, Q. Y. Hao, S. Liu, L. B. Chen and T. H. Wang, *J. Phys. Chem. C*, 2010, **114**, 8084–8088.
28 G. Zhang and X. W. D. Lou, *Angew. Chem., Int. Ed.*, 2014, **126**, 9187–9190.
29 H. Liu, G. Wang, J. Liu, S. Qiao and H. Ahn, *J. Mater. Chem.*, 2011, **21**, 3046–3052.
30 X. Hu, Y. Li, G. Zeng, J. Jia, H. Zhan and Z. Wen, *ACS Nano*, 2018, **12**, 1592–1602.
31 S. H. Choi, Y. N. Ko, J.-K. Lee and Y. C. Kang, *Adv. Funct. Mater.*, 2015, **25**, 1780–1788.
32 S. H. Choi and Y. C. Kang, *Nanoscale*, 2016, **8**, 4209–4216.
33 D. Mcnulty, H. Geaney, D. Buckley and C. O'Dwyer, *Nano Energy*, 2018, **43**, 11–21.
34 Y. Qi, H. Zhang, N. Du, C. Zhai and D. Yang, *RSC Adv.*, 2012, **2**, 9511–9516.
35 C. Yuan, H. B. Wu, Y. Xie and X. W. D. Lou, *Angew. Chem., Int. Ed.*, 2014, **53**, 1488–1504.
36 C. T. Cherian, M. Reddy, S. C. Haur and B. Chowdari, *ACS Appl. Mater. Interfaces*, 2013, **5**, 918–923.
37 S. Niu, W. Lv, C. Zhang, F. Li, L. Tang, Y. He, B. Li, Q.-H. Yang and F. Kang, *J. Mater. Chem. A*, 2015, **3**, 20218–20224.
38 J. Song, M. L. Gordin, T. Xu, S. Chen, Z. Yu, H. Sohn, J. Lu, Y. Ren, Y. Duan and D. Wang, *Angew. Chem., Int. Ed.*, 2015, **127**, 4399–4403.
39 S. Xiao, S. Liu, J. Zhang and Y. Wang, *J. Power Sources*, 2015, **293**, 119–126.
40 J. Zhang, Y. Cai, Q. Zhong, D. Lai and J. Yao, *Nanoscale*, 2015, **7**, 17791–17791.
41 B. Wang, S. Li, X. Wu, W. Tian, J. Liu and M. Yu, *J. Mater. Chem. A*, 2015, **3**, 13691–13698.
42 Q. Zhang, Y. Deng, Z. Hu, Y. Liu, M. Yao and P. Liu, *Phys. Chem. Chem. Phys.*, 2014, **16**, 23451–23460.
43 G. H. Smudde Jr. and P. C. Stair, *Surf. Sci.*, 1994, **317**, 65–72.
44 A. P. Grosvenor, M. C. Biesinger, R. S. C. Smart and N. S. Mcintyre, *Surf. Sci.*, 2006, **600**, 1771–1779.
45 L. Huang, W. Zhang, J. Xiang and Y. Huang, *J. Materiomic*, 2016, **2**, 248–255.
46 B. Wang, Y. Cao, Y. Chen, X. Lai, J. Peng, J. Tu and X. Li, *Nanotechnology*, 2016, **28**, 25501.
47 S.-K. Park, J. K. Kim and Y. C. Kang, *Chem. Eng. J.*, 2017, **328**, 546–555.
48 M. Yao, Z. Hu, Y. Liu and P. A. Liu, *Ionics*, 2016, **22**, 701–709.
49 J.-S. Park, J. S. Cho and Y. C. Kang, *J. Power Sources*, 2018, **379**, 278–287.
50 X. Zhao, J. Sui, F. Li, H. Fang, H. Wang, J. Li, W. Cai and G. Cao, *Nanoscale*, 2016, **8**, 17902–17910.
51 M. Umeda, K. Dokko, Y. Fujita, M. Mohamedi, I. Uchida and J. Selman, *Electrochim. Acta*, 2001, **47**, 885–890.
52 Y. Xu, Y. Zhu, Y. Liu and C. Wang, *Adv. Energy Mater.*, 2013, **3**, 128–133.
53 X. Zhou, J. Bao, Z. Dai and Y.-G. Guo, *J. Phys. Chem. C*, 2013, **117**, 25367–25373.
54 A. D. Roberts, X. Li and H. Zhang, *Chem. Soc. Rev.*, 2014, **43**, 4341–4356.
55 Z. Ding, L. Zhao, L. Suo, Y. Jiao, S. Meng, Y.-S. Hu, Z. Wang and L. Chen, *Phys. Chem. Chem. Phys.*, 2011, **13**, 15127–15133.
56 X. Gu, C. Yan, L. Cao, F. Niu, D. Liu, P. Dai, L. Li, J. Yang and X. Zhao, *J. Mater. Chem. A*, 2017, **5**, 24645–24650.
57 M. S. Jo, G. D. Park, Y. C. Kang and J. S. Cho, *Nanoscale*, 2018, **10**, 13539–13547.
58 X. Gu, P. Dai, L. Li, J. Li, D. Li, H. Zhang and X. Zhao, *ChemistrySelect*, 2016, **1**, 6442–6447.
59 X. Gu, L. Li, Y. Wang, P. Dai, H. Wang and X. Zhao, *Electrochim. Acta*, 2016, **211**, 77–82.
60 Q. Zhang, X. Jiang, K. Liu, H. Qin, L. Li, H. Zheng, S. Wang, C. Feng and G. Li, *J. Nanosci. Nanotechnol.*, 2016, **16**, 7662–7668.